University of Glasgow

Jiang, Y., Liu, P., Chen, Y., Zhou, Z., Yang, H., Hong, Y., Li, F., Ni, L., Yan, Y., and Gregory, D. (2017) Construction of stable Ta3N5/g-C3N4 metal/non-metal nitride hybrids with enhanced visible-light photocatalysis. *Applied Surface Science*, 391, pp. 392-403. (doi:10.1016/j.apsusc.2016.04.094)

This is the author's final accepted version.

There may be differences between this version and the published version. You are advised to consult the publisher's version if you wish to cite from it.

http://eprints.gla.ac.uk/123441/

Deposited on: 29 August 2016

Enlighten – Research publications by members of the University of Glasgow
http://eprints.gla.ac.uk

Construction of stable Ta_3N_5/g-C_3N_4 metal/non-metal nitride hybrids with enhanced visible-light photocatalysis

Yinhua Jiang[a,*], Peipei Liu[a], YeCheng Chen[a], Zhengzhong Zhou[a], Haijian Yang[a], Yuanzhi Hong[b], Fan Li[b], Liang Ni[b] , Yongsheng Yan[a], Duncan H Gregroy[c,*]

a. School of Chemistry and Chemical Engineering, Jiangsu University, Zhenjiang, 2120013，P. R. China

b. School of Materials Science and Engineering, Jiangsu University, Zhenjiang, 2120013，P. R. China

c. School of chemistry, University of Glasgow, Glasgow G12 8QQ, UK

**Corresponding author:*

Tel.: +86 51188791708 *Fax: +86 51188791800*

E-mail address: yms418@126.com (Y.H.Jiang); duncan.gregory@glasgow.ac.uk (D.H Gregory)

Abstract

In this paper, a novel Ta_3N_5/g-C_3N_4 metal/non-metal nitride hybrid was successfully synthesized by a facile impregnation method. The photocatalytic activity of Ta_3N_5/g-C_3N_4 hybrid nitrides was evaluated by the degradation of organic dye rhodamine B (RhB) under visible light irradiation, and the result indicated that all Ta_3N_5/g-C_3N_4 samples exhibited distinctly enhanced photocatalytic activities for the degradation of RhB than pure g-C_3N_4. The optimal Ta_3N_5/g-C_3N_4 composite sample, with Ta_3N_5 mass ratio of 2%, demonstrated the highest photocatalytic activity, and its degradation rate constant was 2.71 times as high as that of pure g-C_3N_4. The enhanced photocatalytic activity of this Ta_3N_5/g-C_3N_4 metal/metal-free nitride was predominantly attributed to the synergistic effect which increased visible-light absorption and facilitated the efficient separation of photoinduced electrons and holes. The Ta_3N_5/g-C_3N_4 hybrid nitride exhibited excellent photostability and reusability. The possible mechanism for improved photocatalytic performance was proposed. Overall, this work may provide a facile way to synthesize the highly efficient metal/metal-free hybrid nitride photocatalysts with promising applications in environmental purification and energy conversion.

Keywords: Ta_3N_5; g-C_3N_4; metal/non-metal nitride hybrids; visible-light photocatalytic activity; synergistic effect; photostability

1. Introduction

In recent years, semiconductor-based photocatalysis has aroused much interest to address the issues of environmental organic pollution and energy crisis, owing to its 'green' nature [1-4]. A large number of semiconductor photocatalysts, such as TiO_2, ZnO, Ta_2O_5 etc, have been extensively investigated. Among these photocatalysts, TiO_2 is the first and the most popular photocatalyst; however, its wide band gap (3.2 eV) limits its applications since it can only be active under ultraviolet (UV) irradiation, which occupies no more than 5% of the solar spectrum [5-6]. In order to effectively utilize the abundant energy from sunlight, numerous efforts have been focused on the development of visible-light responsive semiconductor photocatalysts including g-C_3N_4 [7], Bi_2WO_6 [8], $BiVO_4$ [9], CdS [10], Ta_3N_5 [11], etc. However, single photocatalyst shares some inherent drawbacks such as rapid charge recombination, poor stability and limited visible-light responsive range, and further enhancement in photocatalytic efficiency becomes rather difficult. Therefore, the design and synthesis of composite photocatalysts consisting of matched compounds with superior efficiency for decomposing organic pollutants seem to be a great challenge for the environmental researchers.

Metal nitrides are one of the promising candidates due to their low-cost, good electrical-thermal stability, high photocatalytic activity and noble-metal-like electron feature [12-15]. Moreover, compared with its corresponding oxide, metal nitride often possesses a relatively narrower band gap owing to its more negative potential of the nitrogen 2p orbital than that of the oxygen 2p orbital, resulting in potentially

encompassing nearly the entire solar spectrum [16]. Therefore, metal nitrides can function as visible-light-responsive photocatalysts. Among metal nitrides, tantalum (V) nitride (Ta_3N_5) as an effective visible-light-driven photocatalyst has attracted increasing attention due to its band gap of 2.08 eV, which allows for the absorption of visible light with wavelengths up to 600 nm [11,13]. The prospective candidate Ta_3N_5 has been used in the field of the solar water splitting and decomposition of toxic organic molecules [17-18]. However, nitrogen anions in Ta_3N_5 can readily be oxidized to N_2 by photogenerated holes during the photocatalytic process, so bare Ta_3N_5 shows poor photocatalytic activity and stability, which hinders its practical applications [19-20]. To improve the photocatalytic activity and stability of Ta_3N_5, a strategy must be designed for prompting separation of the photogenerated electrons and holes in the Ta_3N_5 catalyst. One effective method is to couple Ta_3N_5 with other semiconductors to form composites. For example, Adhikari et al. synthesized Ta_3N_5/Bi_2O_3 composites and found that the formation of composites led to increased life time of the electron-hole pairs, enhancing the photocatalytic activity of Ta_3N_5 [21]. Liao et al. prepared Co_3O_4 nanoparticles loaded Ta_3N_5 composite photoanode and demonstrated that Co_3O_4 nanoparticles assisted in releasing the photogenerated holes accumulated on the Ta_3N_5, thus improving the photostability and performance of Ta_3N_5 [19]. Wang et al. synthesized a novel 3D p-n Ag_3PO_4/Ta_3N_5 photocatalyst with enhanced photocatalytic activities in situ template-free method [22]. Nevertheless, in the modification of Ta_3N_5 system, it is still of great interest to find more appropriate compounds to further enhance the photocatalytic performance and stability of Ta_3N_5.

Recently, a metal-free, graphite-like carbon nitride (g-C_3N_4) has been extensively employed in environmental applications since Wang et al. first reported its photocatalytic property under visible light irradiation for hydrogen or oxygen production by water splitting in 2009 [7,23,24]. This carbon nitride is thermally stable and has a narrow band gap of ~2.7 eV owing to the À-conjugated graphitic planes consisted of the sp^2 hybridization of the carbon and nitrogen, so it responds to visible light with wavelengths up to 460 nm [24-26]. However, the photocatalytic activity of individual g-C_3N_4 is restricted because of the fast recombination of photogenerated electron-hole pairs, poor quantum efficiency and the relatively narrow range of photon-response (as it absorbs irradiation with wavelength shorter than 460nm only) [27]. Therefore, it is of great value to extend the light absorption of g-C_3N_4 up to a larger portion of the available solar spectrum and retard the recombination of electron and hole. Material scientists have devoted their efforts to improve the photocatalytic activity of g-C_3N_4 under visible light irradiation by coupling g-C_3N_4 with other materials, in that the planer conjugation structure of g-C_3N_4 can furnish a scaffold to anchor various substrates [26]. A large number of C_3N_4-based composite photocatalysts such as C_3N_4-TiO_2 [28], C_3N_4-SnS_2 [25], Co_3O_4-g-C_3N_4 [23], C_3N_4-Bi_2WO_6 [29] and C_3N_4-$SrTiO_3$ [30], etc have thence been synthesized. These works demonstrated the significantly enhanced photocatalytic activity of the g-C_3N_4 by forming composite structures. In light of the superiorities of Ta_3N_5 and g-C_3N_4 mentioned above, if metal-free g-C_3N_4 couples with metal nitride Ta_3N_5 to form hybrid materials, the photocatalytic activity of the Ta_3N_5/g-C_3N_4 hybrid nitrides is

expected to be greatly enhanced by the synergistic effect. Moreover, the band edges of g-C_3N_4 (E_{CB} = -1.14 eV, E_{VB} = 1.59 eV) match well with those of Ta_3N_5 (E_{CB} = -0.19 eV, E_{VB} = 1.89 eV) overlapping band-structures [31,21]. The well-aligned straddling band structures in Ta_3N_5/g-C_3N_4 hybrid nitrides can efficiently separate and transfer photogenerated electron-hole pairs, which releases the photogenerated holes accumulated on the Ta_3N_5, so the photostability of Ta_3N_5 can be greatly improved. To the best of our knowledge, there is no report on the preparation and investigation of such metal-free nitride/metal nitride hybrid system.

Herein, the synthesis of novel metal/non-metal nitride hybrids consisting of g-C_3N_4 and Ta_3N_5 by a facile impregnation method was reported. The as-prepared Ta_3N_5/g-C_3N_4 composites exhibit greatly enhanced photocatalytic activities towards the decomposition of organic dye rhodamine B (RhB) under visible light irradiation compared with g-C_3N_4. The optimization of experimental condition was investigated in detail and the mechanism of enhanced photocatalytic activity was also proposed. This novel Ta_3N_5/g-C_3N_4 hybrid nitride photocatalysts as promising photocatalytic materials can be potentially used for settling the issue of environmental organic pollution.

2. Experimental

2.1. Materials

Melamine, tantalum oxide (Ta_2O_5, Alfa Aesar, 99.99% metals basis), triethanolamine(TEOA), 1,4-benzoquinone (BQ), iso-propanol (IPA), ethanol and Rhodamine B (RhB) ($C_{28}H_{31}ClN_2O_3$, ≥95%) were of analytical grade and used

without further purification. Ammonia gas was supplied by Pujiang Gas Co., Ltd (Shanghai, China). The deionized water was used throughout this research.

2.2. Photocatalyst preparation

2.2.1. Preparation of carbon nitride and tantalum nitride

Bulk g-C_3N_4 powders were synthesized by themolysis of melamine according to the reported literature [32]. In a typical synthesis, 5 g of melamine was put into an alumina crucible with a cover, and then heated to 550℃ for 4 h in a muffle furnace at a heating rate of 2.3 °C/min. After cooling to room temperature, yellow product was collected and ground in an agate mortar for further use. Ta_3N_5 was fabricated via thermal nitridation of commercial Ta_2O_5 powder at 1023 K for 8 h under anhydrous ammonia gas flow (60mL‡min^{-1}) according to a reported literature [33].

2.2.2. Preparation of Ta_3N_5/g-C_3N_4 hybrids

Ta_3N_5/g-C_3N_4 hybrids photocatalysts were prepared by a facile impregnation method. Specifically, calculated amounts of pure g-C_3N_4 and Ta_3N_5 were added into aqueous ethanol solutions, respectively, and then both were sonicated separately for 30 min. Afterwards, Ta_3N_5 suspension was dropwise added into g-C_3N_4 suspension under continuous ultrasonic agitation. The mixture was then sealed and stirred for one day before volatilization of ethanol and water. The resultant powders were harvested by drying at 80 °C under vacuum. Ta_3N_5 mass content in the Ta_3N_5/g-C_3N_4 hybrid nitrides ranged from 1 to 3 wt% with respect to g-C_3N_4, and the corresponding samples were labeled as 1-Ta_3N_5/g-C_3N_4, 2-Ta_3N_5/g-C_3N_4, and 3-Ta_3N_5/g-C_3N_4 respectively. Pure g-C_3N_4 was treated for the purpose of comparison under the same

experimental conditions.

2.3. Characterization

A D/MAX-2500 diffractometer was used to perform X-ray powder diffraction (XRD) analysis of all as-prepared photocatalysts using Cu K± radiation over the range of 2¸ = 5-80° at the scan rate of 5æmin^{-1} at room temperature, to examine the phase compositions and crystal structures of samples. Fourier transform infrared spectroscopy (FTIR) was performed on a Nicolet-560 FT-IR Spectrometric Analyzer using KBr pellet. The surface chemical composition and chemical states of the catalysts were identified by the X-ray photoelectron spectroscopy (XPS) with a Thermo ESCALAB 250X (America) electron spectrometer using 150 W Al K± X-ray sources. The transmission electron microscopy (TEM: JEM-2010, Japan) and High angle angular dark field-scanning transmission electron microscopy were conducted to characterize the samples by transmission electron microscopy (Tenai G2 F30 S-Twin, FEI) at an acceleration voltage of 20 kV. UV-vis diffuse reflection spectroscopy (DRS) was recorded on a UV-2450 spectrophotometer (Shimadzu Corporation, Japan) with $BaSO_4$ as the reference. Photoluminescence (PL) measurements were carried out on a Perkin-Elmer LS 55 at room temperature with the excitation wavelength of 350 nm. Photocurrent was measured on an electrochemical workstation (CHI 660B Chenhua Instrument Company). Photocatalytic activities were detected on a GHX-3 photochemical reaction instrument.

2.4. Photocatalytic and active species trapping experiments

The photocatalytic activities of as-prepared Ta_3N_5/g-C_3N_4 hybrid photocatalysts

were assessed by the photocatalytic degradation of RhB under visible light irradiation using a 250 W Xenon lamp with a cutoff filter (» > 420 nm). In each experiment, the photocatalysts of ca. 0.05g were put into 50 mL 10 mg/L of RhB aqueous solution. Prior to the photoreactions, the suspension solution was magnetically stirred in the dark for 30 min to establish the adsorption-desorption equilibrium. During visible light irradiation, 3 mL of the suspension was collected at regular time intervals (30 min), and separated by centrifugation (10000 rpm, 15 min) to obtain the RhB supernatant. The RhB concentration was then analyzed with a UV-vis spectrophotometer (Shimadzu, TU-1810) at 553 nm. The active species in the photocatalytic process could be detected by trapping experiment with triethanolamine (TEOA), 1, 4-benzoquinone (BQ), iso-propanol (IPA), which was similar to the photodegradation experiment except that a quantity of scavengers were introduced into the RhB solution prior to the addition of the catalyst. All the experiments were carried out under ambient conditions.

3. Results and discussion

3.1. Characterization of as-prepared samples

The crystalline structures and phases of as-formed Ta_3N_5/g-C_3N_4 photocatalysts were characterized by XRD. As illustrated in Fig. 1, the XRD pattern of pure Ta_3N_5 shows that all the diffraction peaks (marked with •Ï •) can be indexed to the orthorhombic Ta_3N_5 (01-079-1533) [34]. For pure g-C_3N_4, the identified peaks at 13.1° and 27.4° correspond to the (100) and (002) (marked with • f •) diffraction planes, respectively (JCPDS 87-1526) [35]. The former is associated with the interlayer

structural packing, and the latter is related to the stacking of the conjugated aromatic system [27,36]. As for the Ta_3N_5/g-C_3N_4 composites, the XRD patterns display the combination of two sets of diffraction data for both g-C_3N_4 and Ta_3N_5. With the increase of Ta_3N_5 content, the intensities of the Ta_3N_5 peaks are gradually enhanced at the expense of g-C_3N_4 peaks. The main characteristic diffraction peak positions of Ta_3N_5/g-C_3N_4 composites do not obviously change after Ta_3N_5 being hybridized with g-C_3N_4. However, the peak at $2\theta=28.3^{\circ}$ corresponding to the (112) crystal plane of Ta_3N_5 is concealed by the strong peak of g-C_3N_4. Moreover, there is no other impurity phase discovered. The result confirms that Ta_3N_5/g-C_3N_4 hybrid photocatalysts are composed of Ta_3N_5 and g-C_3N_4.

To further investigate the hybrid combination and interaction between g-C_3N_4 and Ta_3N_5 in Ta_3N_5/g-C_3N_4 hybrid nitrides, the FT-IR spectroscopy was carried out and the results are shown in Fig. 2. In the case of Ta_3N_5, the peak at 890 cm^{-1} observed is attributed to the characteristic absorption band of the Ta-N bond [34]. As for pure g-C_3N_4, the peak at 810 cm^{-1} arises from the breathing mode of s-triazine ring [32]. Several strong bands in the 1240-1640 cm^{-1} region are also found in the spectrum. The peaks at 1241, 1323, 1409, and 1568 cm^{-1} correspond to aromatic C-N stretching vibrations, while the peak at 1638 cm^{-1} is related to the typical stretching vibration mode of the C=N [37-38]. The broad band centered at 3217 cm^{-1} is related to the N-H stretching vibration of residual amine with the sp^2-hybridized carbon and intermolecular hydrogen-bonding interactions [39]. As for the Ta_3N_5/g-C_3N_4 composites, the main peaks of g-C_3N_4 and Ta_3N_5 are all present and no other new

chemical bonds are seen, suggesting the co-existence of g-C_3N_4 and Ta_3N_5 in the catalyst. Moreover, the intensity of absorption peaks first increase and then decrease with increasing Ta_3N_5 content, which suggests that 2-Ta_3N_5/g-C_3N_4 has the richest superficial bands with high surface reaction performance, especially in the range of 1240-1640 cm^{-1}. Additionally, it can also be noted that there is a slight red shift in the characteristic peak of the Ta-N stretching vibration in Ta_3N_5/g-C_3N_4 composites, implying the strong covalent interaction between g-C_3N_4 and Ta_3N_5, which agrees well with Wang's report [40].

XPS technique is a very important method to investigate the chemical composition and states of the as-prepared photocatalysts. The survey scan XPS spectra of the pure g-C_3N_4 and 2-Ta_3N_5/g-C_3N_4 photocatalyst are shown in Fig. 3. The peaks of C 1s, N 1s, and O 1s representing the carbon, nitrogen and a small amount of oxygen are present in the spectra of both pure g-C_3N_4 and 2-Ta_3N_5/g-C_3N_4. The oxygen might be absorbed from the atmosphere during the survey scan [44]. For 2-Ta_3N_5/g-C_3N_4, in addition to the peaks of C 1s, N 1s, and O 1s, the peaks representing Ta 4f are also detected in the XPS spectrum.

The high-resolution XPS spectra of C 1s, N 1s, O 1s and Ta 4f are shown in Fig. 4. As can be seen from C 1s spectra (Fig. 4a), the C peaks at the binding energy of 284.6 and 288.1 eV for g-C_3N_4 are assigned to surface adventitious carbon and defect-containing sp^2-bonded carbon, respectively [27,41]. The C ls spectrum of 2-Ta_3N_5/g-C_3N_4 is similar to that of g-C_3N_4, but the peak at 288.1 eV in g-C_3N_4 for defect-containing sp^2-bonded carbon shifts 0.4 eV towards lower binding energy

(287.7 eV). According to the N 1s spectra (Fig. 4b), the N 1s curve of g-C_3N_4 can be deconvoluted into three peaks, locating at 396.5, 398.5 and 400.1 eV, respectively. The peak at 396.5 eV is assigned to the sp^2-hybridized N nitrogen (C=N-C), conforming the presence of sp^2-bonded graphitic carbon nitride. The peaks at 398.5 and 400.1 eV are derived from the bridging tertiary nitrogen N-$(C)_3$ and N atoms in amino groups (C-N-H), respectively. Comparatively, the N 1s band of 2-Ta_3N_5/g-C_3N_4 composite can be fitted to four peaks at 395.6, 397.0, 398.5 and 400.1 eV, respectively. The asymmetrical features of N 1s XPS spectrum for 2-Ta_3N_5/g-C_3N_4 imply the coexistence of a number of distinguishable nitrogen models. The new peak at 395.6 eV is ascribed to the N^{3-} of Ta_3N_5 [22], and the other three peaks at 397.0, 398.5 and 400.1 eV are resulted from g-C_3N_4. Moreover, the binding energy at 397.0 eV of N ls for C=N-C in 2-Ta_3N_5/g-C_3N_4 composite positively shifts by 0.5 eV compared with that of g-C_3N_4 [37,42]. The above results confirm that Ta_3N_5 and g-C_3N_4 hybrids have been successfully synthesized. And the shifts in C1s and N 1s suggest the covalent interaction between Ta_3N_5 and g-C_3N_4. Such similar phenomenon has been reported [43]. The O1s XPS traces of g-C_3N_4 and 2-Ta_3N_5/g-C_3N_4 (Fig. 4c) show that the binding energy peak of O 1s at ~532 eV observed is associated with the adsorbed water molecules from the atmosphere in samples [44]. The Ta 4f peaks in Fig. 4d at 25.93 and 23.01 eV correspond to Ta $4f_{5/2}$ and Ta $4f_{7/2}$ orbitals of Ta^{5+} in 2-Ta_3N_5/g-C_3N_4, respectively [45].

The morphology and microstructure of Ta_3N_5, g-C_3N_4 and 2-Ta_3N_5/g-C_3N_4 samples were characterized by FE-SEM and TEM as shown in Fig. 5. From Fig. 5a

and 5b, it is obvious that Ta_3N_5 agglomeration have cuboid-like structures with well-defined faces, while pure g-C_3N_4 is composed of agglomerated morphologies with a large size and smoothly stacking flakiness layers [25,46]. After inducing Ta_3N_5 to g-C_3N_4, 2-Ta_3N_5/g-C_3N_4 composite consists of irregular agglomeration architectures. It can be found that cuboid-like Ta_3N_5 structures are assembled onto the surface of g-C_3N_4 (Fig. 5c), implying the coexistence of Ta_3N_5 and g-C_3N_4 where the heterojunction is formed at the interface of Ta_3N_5/g-C_3N_4 hybrids. The TEM image (Fig. 5d) demonstrates that individual Ta_3N_5 is composed of irregular nanosized blocky structure with well-defined outlines. Pure g-C_3N_4 reveals an ultrathin sheet structure with a big superficial area (Fig. 5e). The corresponding TEM image of 2-Ta_3N_5/g-C_3N_4 composite shows the coexistence of two distinct structures of light-colored straticulate g-C_3N_4 layer and dark Ta_3N_5 nanosized block (Fig. 5f). More attractively, the cuboid-like Ta_3N_5 are attached to the surface of g-C_3N_4 sheets, which is responsible for the transfer of electrons and holes between g-C_3N_4 and Ta_3N_5. In order to further explore the distribution and coexistence of elements present, the EDX mappings of sample 2-Ta_3N_5/g-C_3N_4 composite were carried out. As shown in Fig. 6, C, N and Ta species were all detected in Ta_3N_5/g-C_3N_4 composite sample, in which a spot of Ta element and a mass of C, N elements were seen. And all elemental distributions give solid evidence that Ta_3N_5 are well attached to the surface of g-C_3N_4 sheets g-C_3N_4 sheets, forming heterojunction.

Full nitrogen sorption isotherms were measured to learn more about specific surface area and pore characteristic of pure g-C_3N_4 and 2-Ta_3N_5/g-C_3N_4 composite. As

shown in Fig. 7, the isotherm for g-C_3N_4 and 2-Ta_3N_5/g-C_3N_4 are categorized as type IV with a typical H3 type hysteresis loop according to the IUPAC classification, reflecting that the mesoporous structure are formed due to the irregular agglomeration of the plate-like samples. The corresponding pore size distribution curves using Barrett-Joyner-Halenda (BJH) analyses (the inset in Fig. 7) illustrate that pore sizes of samples are all concentrated at 2-7 nm. For clear comparison, the specific surface area, pore volume and pore size distribution of g-C_3N_4 and 2-Ta_3N_5/g-C_3N_4 are summarized in Table 1. It can be found that the BET surface area (S_{BET}) of pure g-C_3N_4 is of 47.813 m^2 g^{-1}. Compared with pure g-C_3N_4, the 2-Ta_3N_5/g-C_3N_4 exhibits a significant decreased surface area of 14.475 m^2 g^{-1}. The reason may be that cuboid-like Ta_3N_5 structures dispersing onto the surface of g-C_3N_4 should block some part surfaces of g-C_3N_4 [1,58]. From the result, it can be known that the BET surface area is not the main factor in enhancing the photocatalytic activity in Ta_3N_5/g-C_3N_4 system.

The optical absorption property is an important factor to influence the photocatalytic activity of the catalysts. Thus, the absorbance properties of as-prepared samples were analyzed by the UV-vis diffuse reflection spectra (DRS), and the results are shown in Fig. 8a. From Fig. 8a, pure g-C_3N_4 shows the absorbance from UV to visible range up to 460 nm due to its intrinsic band gap energy of 2.7 eV [26,47]. The absorption onset of Ta_3N_5 with the band-gap value of 2.08 eV is found at approximately 620 nm, which exhibits the broad absorption region of visible-light [34]. Compared with pure g-C_3N_4, the absorption abilities of Ta_3N_5/g-C_3N_4 composites are obviously enhanced in the visible-light region due to the presence of

Ta_3N_5. And the absorption edges of Ta_3N_5/g-C_3N_4 composites show red shifts step by step with the increasing Ta_3N_5 content, which corresponds to the color changes of composites (the inset in Fig. 8a). The color of pure g-C_3N_4 and Ta_3N_5 are light yellow and deep red, respectively. And the color changes of hybrid nitrides (from 1-Ta_3N_5/g-C_3N_4 to 3-Ta_3N_5/g-C_3N_4) are from cream to cream-pink as the Ta_3N_5 content increased. The results suggest that all Ta_3N_5/g-C_3N_4 photocatalysts might possess higher photocatalytic performances than pure g-C_3N_4 for their strong visible light responsive. In addition, the optical band gap energy of samples was estimated by the following formula:

$$\pm h\nu = A(h\nu - E_g)^{n/2} \quad (1)$$

Where ± represents the absorption coefficient, h is Planck's constant, ν is light frequency, A and E_g are proportionality and band gap energy, respectively. The value of n is determined by the transition modes of semiconductors such as indirect transition (n=1) and direct transition (n=4). According to previous studies, n values of g-C_3N_4 and Ta_3N_5 are 4 and 1, respectively. For pure g-C_3N_4, the band gap was obtained from a plot of $(\pm h\nu)^{1/2}$ versus $h\nu$ [31], and the band gap of Ta_3N_5 was determined by a plot of $(\pm h\nu)^2$ versus $h\nu$ [48]. As illustrated in Fig. 8b, the band gaps of Ta_3N_5 and g-C_3N_4 were evaluated to be 2.08 eV and 2.73 eV, respectively, which closely agree with the previous reports [34,26]. The energy band gaps of Ta_3N_5/g-C_3N_4 hybrid nitrides (from 1-Ta_3N_5/g-C_3N_4 to 3-Ta_3N_5/g-C_3N_4) were estimated to be 2.72, 2.69 and 2.68 eV from the plots of $(\pm h\nu)^{1/2}$ versus $h\nu$, respectively. Obviously, the presence of Ta_3N_5 contributes to the red shift of the

absorption onset, resulting in the narrow band gaps of Ta_3N_5/g-C_3N_4 hybrid nitrides.

3.2. Photocatalytic activity and stability

Organic dye RhB was used as a model pollutant to evaluate the photocatalytic activities of as-obtained photocatalysts under visible-light irradiation. As shown in Fig. 9a, the photolysis of RhB without any catalyst is negligible as the RhB concentration is almost unchanged. With the addition of pure g-C_3N_4, the degradation ratio of RhB is up to 66.61% after 3 h irradiation, attributing to its appropriate band gap (2.7 eV) and unique electronic structure [36]. Further enhancements in photocatalytic activity is exhibited by the composite catalyst Ta_3N_5/g-C_3N_4, owing to the synergetic effects of the two components that result in the increased visible-light absorption and the efficient separation of electron-hole pairs between g-C_3N_4 and Ta_3N_5. Remarkably, the mass content of Ta_3N_5 has a great influence on the photocatalytic activities of the composites. The Ta_3N_5/g-C_3N_4 hybrid nitride with 2wt.% of Ta_3N_5 possesses the highest photocatalytic activity (94.43% degradation of RhB after 3h irradiation), while Ta_3N_5 loading over 2wt. % decreases the performance. The reason could be that the excess Ta_3N_5 might form aggregates, which blocked the transfer of electrons and holes between g-C_3N_4 and the Ta_3N_5.

In order to investigate the kinetics of RhB degradation by as-prepared Ta_3N_5/g-C_3N_4 hybrids, the pseudo-first-order equation was used to analyze the experiment data as follows:

$$ln(C_0/C) = kt \quad (2)$$

Where k is the apparent pseudo-first-order rate constant, C_0 and C are the initial

concentration at t=0 and the instantaneous concentration of RhB remaining in the solution at irradiation time t respectively. As shown in Fig. 8b, the plots of the irradiation time (t) against $ln(C_0/C)$ are nearly straight lines, confirming that the photodegradation reaction is indeed pseudo-first-order. The pseudo-first-order rate constants of composites determined from the slopes of plots (Fig. 9b) are displayed in Fig. 9c, it can be easily observed that the values of kinetic rate constant of all Ta_3N_5/g-C_3N_4 hybrids are much higher than that of g-C_3N_4. The highest rate constant k of 2-Ta_3N_5/g-C_3N_4 is 0.9757 h^{-1}, which is 2.71 times as high as that of pure g-C_3N_4 (0.3601 h^{-1}). From these results, it is very clear that the photocatalytic activity of Ta_3N_5/g-C_3N_4 can be significantly improved after coupling g-C_3N_4 with Ta_3N_5.

In the presence of 2-Ta_3N_5/C_3N_4 photocatalyst, the temporal absorption spectra changes of RhB after different degradation time are presented in Fig. 9d. Obviously, the characteristic maximum absorption peak (553 nm) decreased sharply and almost vanished after 3h visible irradiation. It can be also found the main absorption peak of RhB blue shifted from 553 to 498 nm during the degradation, and the blue shifted absorption peak almost disappeared with the increase of irradiation time to 3h. The results demonstrate that the conjugated chromophoric structure of the RhB dye is completely destructed and the gradual hypsochromic shifts occurred is related to the step-by-step *N*-deethylation of RhB during the reaction [49]. According to previous reports [50], the intermediates generated using RhB as the model pollutant under visible-light irradiation are in turn to *N*,*N*,*N'*-triethyl rhodamine, *N*,*N'*-diethyl rhodamine, *N*-ethylrhodamine and rhodamine corresponding to 539, 522 , 510 and

498 nm, respectively.

The photostability and reusability of the as-prepared photocatalyst are critical parameters for practical applications, and were examined by repeatedly running RhB degradation experiments using the same photocatalyst. The experimental conditions were set at which the optimal degradation rate was obtained. Fig. 10 shows the photocatalytic activity of 2-Ta_3N_5/g-C_3N_4 composite decreases only slightly (90.06% remaining) after four successive runs under visible light irradiation, which could be due to the slight loss of photocatalyst during the experiment. The result above demonstrates a relatively long lifetime of 2-Ta_3N_5/g-C_3N_4, implying that the synthesized photocatalyst possesses high photostability for its practical application.

3.3. Charge transfer and separation properties

The transfer and separation efficiency of photogenerated electron-hole pairs were estimated by photoluminescence (PL) spectra analysis in as-prepared samples, as shown in Fig. 11. Herein, the PL spectra of pure g-C_3N_4 and Ta_3N_5/g-C_3N_4 composites were excited by irradiation of wavelength 350 nm. It can be seen that the main PL emission peak of pure g-C_3N_4 is at about 460 nm, because the energy of emission light resembles to the E_g of g-C_3N_4 [51], which is in agreement with the result of the UV-vis analysis. When Ta_3N_5 was combined with g-C_3N_4, the emission intensity of Ta_3N_5/g-C_3N_4 composites observed is smaller than that of pure g-C_3N_4 with the emission peak at nearly the same position, and 2-Ta_3N_5/g-C_3N_4 sample has the weakest intensity. Theoretically, smaller PL intensity means lower recombination rate of photo-generated electrons and holes, resulting in higher photocatalytic activity [38].

The findings in PL spectra indicate that the introduction of Ta_3N_5 to g-C_3N_4 can efficiently suppress the recombination of photo-generated charge carrier, and 2-Ta_3N_5/g-C_3N_4 composite possesses the highest separation efficiency of photo-generated electrons and holes.

To further study the charge transfer and separation properties of Ta_3N_5/g-C_3N_4 composites, the photocurrent-time (I-t) measurement of g-C_3N_4 and 2-C_3N_4/Ta_3N_5 photocatalyst was performed for several on-off irradiation cycles in Fig. 12. As can be seen from the curves, the photocurrent generation sharply increases with light irradiation, and the values of photocurrent instantaneously close to zero as soon as the lamp is turned off. After several on-off cycles, the photocurrent values become constant. Meanwhile, the photocurrents are steady and reproducible during the process of photocurrent response [42,36]. In contrast to the pure g-C_3N_4, the transient photocurrent density of 2-C_3N_4/Ta_3N_5 photocatalysts is noticeably improved, which is about two times higher than that of pure g-C_3N_4. It is very clear that the 2-C_3N_4/Ta_3N_5 composite displays remarkably higher current responses, indicating that the 2-Ta_3N_5/g-C_3N_4 photocatalyst has a higher separation rate of photoinduced electrons and holes as well as a faster charge transfer between g-C_3N_4 and Ta_3N_5. As a result, 2-Ta_3N_5/g-C_3N_4 hybrid nitride possesses higher photocatalytic activity than pure g-C_3N_4.

3.4. Photocatalytic mechanism

The different active species such as $\bullet O_2^-$, h^+ and •OH trapping experiments were investigated by the degradation of RhB in the presence of different scavengers to

explore the enhanced photocatalytic mechanism. The triethanolamine (TEOA), 1,4-benzoquinone (BQ) and iso-propanol (IPA) sacrificial agents are applied as the hole (h^+) scavenger, superoxide radical ($\bullet O_2^-$) scavenger, hydroxyl radical (•OH) scavenger, respectively. As shown in Fig. 13, the introduction of TEOA significantly suppresses the photodegradation activity of composite, demonstrating the photogenerated holes play a crucial role in the photocatalytic reaction. The addition of IPA also slightly decreases the photocatalytic activity, whereas BQ only shows a little effect on the photodegradation of RhB, manifesting that •OH is also a minor activated species and $\bullet O_2^-$ almost has no effect on photodegradation of RhB.

On the basis of above discussion, the schematic mechanism of enhanced photocatalytic activity over Ta_3N_5/g-C_3N_4 photocatalysts was tentatively proposed in Fig. 14. It's well known that the band edges potential position of two semiconductors play an important role in studying the flowchart of photo-excited charge carriers in hybrids, which influences photocatalytic performance of as-formed photocatalysts [36]. The potentials of the conduction band (CB) of g-C_3N_4 and Ta_3N_5 were calculated by the following equation of Mulliken electronegativity theory [52]:

$$E_{CB} = Ç - E_0 - 0.5\,E_g \qquad (3)$$

Where *Ç*are 4.73 and 5.35 for g-C_3N_4 and Ta_3N_5, respectively [21,31]. E_0 is the energy of free electrons with the hydrogen scale (4.5 eV), and E_g is the band gap energy. According to the result of UV-Vis absorption spectra, the E_g energy of g-C_3N_4 and Ta_3N_5 were 2.73 and 2.08 eV, respectively. Thus, the conduction band (CB) of g-C_3N_4 and Ta_3N_5 were evaluated to be -1.14 and -0.19 eV versus normal hydrogen electrode

(NHE), respectively. The valence band gap (VB) of g-C_3N_4 and Ta_3N_5 were about 1.59 and 1.89 eV *vs*. NHE, respectively by the following empirical formula:

$$E_{VB} = E_{CB} + E_g \quad (4)$$

When Ta_3N_5 is connected to g-C_3N_4, the Ta_3N_5/g-C_3N_4 hybrid nitrides have the well-aligned straddling band structures due to the matched values of conduction band (CB) and valence bandgap (VB) of Ta_3N_5 and g-C_3N_4 (Fig. 14). Under visible light irradiation, both g-C_3N_4 and Ta_3N_5 can be excited simultaneously to create electrons and holes in the conduction band and valance band for their narrow bandgaps (Eq. 4). The well-aligned straddling band structures endow that the photogenerated electron on the CB of g-C_3N_4 can easily transfer to the CB of Ta_3N_5, which is assigned to the potential of CB of g-C_3N_4 (-1.14 eV) is more negative than that of Ta_3N_5 (-0.19 eV). Meanwhile, the holes on VB of Ta_3N_5 can be injected to the VB of g-C_3N_4. The charge transfer effectively inhibits the recombination of photoproduced electron-hole pairs, and thus enhances the photocatalytic activity. Compared with the standard redox potential of •OH, H^+/H_2O (E^0 (•OH, H^+/H_2O) = 2.7 eV *vs*. NHE) [57], the photoexcited holes (including g-C_3N_4 and Ta_3N_5) on the g-C_3N_4 surface are insufficient to oxidize H_2O to produce •OH radicals due to its more negative VB (1.59 eV). Therefore, the separated holes effectively collected by g-C_3N_4 have the tendency to directly decompose RhB during the process (Eq. 5) [58]. It is worth noting that the holes transferred onto the g-C_3N_4 surface also greatly improve the photostability of Ta_3N_5 because the chance for the oxidation of nitrogen anions in Ta_3N_5 by photogenerated holes significantly is reduced during the photocatalytic process. The

photogenerated electrons moving to Ta_3N_5 are able to react with O_2 to form reactive superoxide radical ions ($\bullet O_2^-$) in that the CB of Ta_3N_5 (-0.19 eV) is more negative than that of $O_2/\bullet O_2^-$ (E^0 ($O_2/\bullet O_2^-$) = -0.046 eV *vs.* NHE) (Eq. 6) [53-56]. Then, the $\bullet O_2^-$ further reduced or disproportionated by one electron, resulting in the formation of H_2O_2 (Eq. 7). And the H_2O_2 can react with the electrons to produce •OH (Eq. 8), which can decompose the RhB molecules (Eq. 9). Based on the above discussion, the charge transfer and the photodegradation of RhB are proposed as follows [59-60]:

$$Ta_3N_5/g\text{-}C_3N_4 + hv' \quad Ta_3N_5/g\text{-}C_3N_4\ (e^- + h^+) \qquad (4)$$

$$h^+ + RhB' \quad \text{degradation products} \qquad (5)$$

$$O_2 + e^-' \quad \bullet O_2^- \qquad (6)$$

$$\bullet O_2^- + e^- + 2H^+' \quad H_2O_2 \qquad (7)$$

$$H_2O_2 + e^-' \quad \bullet OH + OH^- \qquad (8)$$

$$\bullet OH + RhB' \quad \text{degradation products} \qquad (9)$$

Conclusions

In summary, a novel $Ta_3N_5/g\text{-}C_3N_4$ metal/metal-free hybrid nitride was successfully fabricated through a facile impregnation method. The experiment results showed that the introduction of Ta_3N_5 to $g\text{-}C_3N_4$ created synergistic effects that enhanced the visible-light absorption and efficiently retarded the recombination of electron-hole pairs in $Ta_3N_5/g\text{-}C_3N_4$ system, resulting in the superior photoactivity and high photostability of composite. The $Ta_3N_5/g\text{-}C_3N_4$ hybrid nitride with 2 wt. % Ta_3N_5 exhibited the highest photocatalytic efficiency (94.43%) for the degradation of RhB, which was about 2.71 times higher than that of pure $g\text{-}C_3N_4$. This study implied that

this Ta_3N_5/g-C_3N_4 hybrid nitride composite material might have great potential applications in pollutant removal and energy conversion.

Acknowledgements

This research was sponsored by the National Basic Research Program of China (21576214, 21175061 and 31470434), Research Foundation for Advanced Talents of Jiangsu University (10JDG142) and Special Financial Grant from the China Postdoctoral Science Foundation (2014T70488).

References

[1] J. Li, E.Z. Liu, Y.N. Ma, X.Y. Hu, J. Wan, L. Sun, J. Fan, Synthesis of MoS_2/g-C_3N_4 nanosheets as 2D heterojunction photocatalysts with enhanced visible light activity, Appl. Surf. Sci. 364 (2016) 694-702.

[2] D.L. Jiang, L.L. Chen, J.J. Zhu, M. Chen, W.D. Shi, J.M. Xie, Novel p-n heterojunction photocatalyst constructed by porous graphite-like C_3N_4 and nanostructured BiOI: facile synthesis and enhanced photocatalytic activity, Dalton Trans. 42 (2013) 15726-15734.

[3] L.H. Zhang, X.X. Wang, Q.Y. Nong, H.J. Lin, B.T. Teng, Y.T. Zhang, L.H. Zhao, T.H. Wu, Y.M. He, Enhanced visible-light photoactivity of g-C_3N_4 via Zn_2SnO_4 modification, Appl. Surf. Sci. 329 (2015) 143-149.

[4] T. Xian, H. Yang, L.J. Di, J.F. Dai, Enhanced photocatalytic activity of $BaTiO_3$@g-C_3N_4 for the degradation of methyl orange under simulated sunlight irradiation, J. Alloys Compd. 622 (2015) 1098-1104.

[5] J.Q. Wen, X. Li, W. Liu, Y.P. Fang, J. Xie, Y.H. Xu, Photocatalysis fundamentals and surface modification of TiO_2 nanomaterials, Chinese. J. Catal. 36 (2015) 2049-2070.

[6] H. Xu, J.X. Zhu, Y.X. Song, W.K. Zhao, Y.G. Xu, Y.H. Song, H.Y. Ji , H.M. Li, Ion-exchange preparation for visible-light-driven photocatalyst AgBr/Ag_2CO_3 and its photocatalytic activity, RSC Adv. 4 (2014) 9139-9147.

[7] X.C. Wang, K. Maeda, X.F. Chen, K. Takanabe, K. Domen, Y.D. Hou, X.Z. Fu, M. Antonietti, Polymer semiconductors for artificial photosynthesis: hydrogen evolution

by mesoporous graphitic carbon nitride with visible light, J. Am. Chem. Soc. 131 (2009) 1680-1681.

[8] Z.J. Zhang, W.Z. Wang, M. Shang, W.Z. Yin, Low-temperature combustion synthesis of Bi_2WO_6 nanoparticles as a visible-light-driven photocatalyst, J. Hazard. Mater. 177 (2010) 1013-1018.

[9] F.F. Abdi, R.V. Krol, Nature and light dependence of bulk recombination in Co-Pi-catalyzed $BiVO_4$ photoanodes, J. Phys. Chem. C 116 (2012) 9398-9404.

[10] J.Z. Yang, J.W. Yu, J. Fan, D.P. Sun, W.H. Tang, X.J. Yang, Biotemplated preparation of CdS nanoparticles/bacterial cellulose hybrid nanofibers for photocatalysis application, J. Hazard. Mater. 189 (2011) 377-383.

[11] Y.F. Wang, W.H. Ma, C.C. Chen, X.F. Hu, J.C. Zhao, J.C. Yu, Fe^{3+}/Fe^{2+} cycling promoted by Ta_3N_5 under visible irradiation in fenton degradation of organic pollutants, Appl. Catal. B: Environ. 75 (2007) 256-263.

[12] A.M. Alexander, S.J. Hargreaves, Alternative catalytic materials: carbides, nitrides, phosphides and amorphous boron alloys, Chem. Soc. Rev. 39 (2010) 4388-4401.

[13] Y. Li, Q.Y. Feng, H. Wang, G. Zhou, Z.S. Wang, Reduced graphene oxide-Ta_3N_5 composite: a potential cathode for efficient $Co(bpy)_3^{3+/2+}$ mediated dye-sensitized solar cells, J. Mater. Chem. A. 1 (2013) 6342-6349.

[14] X.H. Zhou, C.Q. Shang, L. Gu, S.M. Dong, X. Chen, P.X. Han, L.F. Li, J.H. Yao, Z.H. Liu, H.X. Xu, Y.W. Zhu, G.L. Cui, Mesoporous coaxial titanium

nitride-vanadium nitride fibers of core-shell structures for high-performance supercapacitors, ACS Appl. Mater. Interfaces 3 (2011) 3058-3063.

[15] D.W. Choi, P. N. Kumta, Synthesis, structure, and electrochemical characterization of nanocrystalline tantalum and tungsten nitrides, J. Am. Ceram. Soc. 90 (2007) 3113-3120.

[16] Z. Wang, J.G. Hou, C. Yang, S.Q. Jiao, K. Huang, H.M. Zhu, Hierarchical metastable Y-TaON hollow structures for efficient visible-light water splitting, Energy Environ. Sci. 6 (2013) 2134-2144.

[17] Z.X. Su, S. Grigorescu, L. Wang, K. Lee, P. Schmuki, Fast fabrication of Ta_2O_5 nanotube arrays and their conversion to Ta_3N_5 for efficient solar driven water splitting, Electrochem.Commun. 50 (2015) 15-19.

[18] P. Zhang, J.J. Zhang, J.L. Gong, Tantalum-based semiconductors for solar water splitting, Chem. Soc. Rev. 43 (2014) 4395-4422.

[19] M. Liao, J. Feng, W. Luo, Z. Wang, J. Zhang, Z. Li, T. Yu, Z. Zou, Co_3O_4 nanoparticles as robust water oxidation catalysts towards remarkably enhanced photostability of a Ta_3N_5 photoanode, Adv. Funct. Mater. 22 (2012) 3066-3074.

[20] Y.C. Wang, C.Y. Chang, T.F. Yeh, Y.L. Lee, H. Teng, Formation of internal p-n junctions in Ta_3N_5 photoanodes for water splitting, J. Mater. Chem. A 2 (2014) 20570-20577.

[21] S.P. Adhikari, Z.D. Hood, K.L. More, I. Ivanov, L.F. Zhang, M. Grossab, A. Lachgar, Visible light assisted photocatalytic hydrogen generation by Ta_2O_5/Bi_2O_3, $TaON/Bi_2O_3$, and Ta_3N_5/Bi_2O_3 composites, RSC Adv. 5 (2015) 54998-55005.

[22] W. Wang, H.B. Fang, Y.Z. Zheng, Y.K. Che, X. Tao, J.F. Chen, In situ template-free synthesis of a novel 3D p-n heteroarchitecture Ag_3PO_4/Ta_3N_5 photocatalyst with high activity and stability under visible radiation, RSC Adv. 5 (2015) 62519-62526.

[23] S.Z. Wu, K. Li, W.D. Zhang, On the heterostructured photocatalysts $Ag_3VO_4/g\text{-}C_3N_4$ with enhanced visible light photocatalytic activity, Appl. Surf. Sci. 324 (2015) 324-331.

[24] G.C. Bi, J.Q. Wen, X. Li, W. Liu, J. Xie, Y.P. Fang, W.W. Zhang, Efficient visible-light photocatalytic H_2 evolution over metal-free $g\text{-}C_3N_4$ co-modified via robust acetylene black and $Ni(OH)_2$ as dual co-catalysts. Chem. Soc. Rev. 2016, DOI: 10.1039/C5CS00838G.

[25] L. Liu, Y.H. Qi, J.Y. Yang, W.Q. Cui, X.G. Li, Z.S. Zhang, An $AgI@g\text{-}C_3N_4$ hybrid core@shell structure: stable and enhanced photocatalytic degradation, Appl. Surf. Sci. 358 (2015) 319-327.

[26] D. Lu, G.K. Zhang, Z. Wan, Visible-light-driven $g\text{-}C_3N_4/Ti^{3+}\text{-}TiO_2$ photocatalyst co-exposed {0 0 1} and {1 0 1} facets and its enhanced photocatalytic activities for organic pollutant degradation and Cr(VI) reduction, Appl. Surf. Sci. 358 (2015) 223-230.

[27] H. Xu, J. Yan, Y.G. Xu, Y.H. Song, H.M. Li, J.X. Xia, C.J. Huang, H.L. Wan, Novel visible-light-driven AgX/graphite-like C_3N_4 (X = Br, I) hybrid materials with synergistic photocatalytic activity, Appl. Catal. B: Environ. 129 (2013) 182-193.

[28] N. Tian, H.W. Huang, Y.H. Zhang, Mixed-calcination synthesis of

$CdWO_4$/g-C_3N_4 heterojunction with enhanced visible-light-driven photocatalytic activity, Appl. Surf. Sci. 358 (2015) 343-349.

[29] Y.J. Wang, X.J. Bai, C.S. Pan, J. He, Y.F. Zhu, Enhancement of photocatalytic activity of Bi_2WO_6 hybridized with graphite-like C_3N_4, J. Mater. Chem. 22 (2012) 11568-11573.

[30] X.X. Xu, G. Liu, C. Randorn, J.T.S. Irvine, G-C_3N_4 coated $SrTiO_3$ as an efficient photocatalyst for H_2 production in aqueous solution under visible light irradiation, Int. J. Hydrogen Energy. 36 (2011) 13501-13507.

[31] Y.Z. Hong, Y.H. Jiang, C.S. Li, W.Q. Fan, X. Yan, M. Yan, W.D. Shi, In-situ synthesis of direct solid-state Z-scheme V_2O_5/g-C_3N_4 heterojunctions with enhanced visible light efficiency in photocatalytic degradation of pollutants, Appl. Catal. B: Environ. 180 (2016) 663-673.

[32] L. Liu, Y.H. Qi, J.S. Hu, Y.H. Liang, W.Q. Cui, Efficient visible-light photocatalytic hydrogen evolution and enhanced photostability of core@shell Cu_2O@g-C_3N_4 octahedra, Appl. Surf. Sci. 351 (2015) 1146-1154.

[33] J. Cao, L. Ren, N. Li, C.W. Hu, M.H. Cao, Mesoporous Ta_3N_5 microspheres prepared from a high-surface-area, microporous, amorphous precursor and their visible-light-driven photocatalytic activity, Chem. Eur. J. 19 (2013) 12619-12623.

[34] X.M. Liu, L. Zhao, K. Domen, K. Takanabe, Photocatalytic hydrogen production using visible-light-responsive Ta_3N_5 photocatalyst supported on monodisperse spherical SiO_2 particulates, Mater. Res. Bull. 49 (2014) 58-65.

[35] S.W. Cao, J.X. Low, J.G. Yu, M. Jaroniec, Polymeric photocatalysts based on

graphitic carbon nitride, Adv. Mater. 27 (2015) 2150-2176.

[36] X.C. Wang, K. Maeda, A. Thomas, K. Takanabe, G. Xin, J.M. Carlsson, K. Domen, M. Antonietti, A metal-free polymeric photocatalyst for hydrogen production from water under visible light. Nat. Mater. 8 (2009) 76-80.

[37] A. Akhundi, A. Habibi-Yangjeh, Ternary g-C_3N_4/ZnO/AgCl nanocomposites: synergistic collaboration on visible-light-driven activity in photodegradation of an organic pollutant, Appl. Surf. Sci. 358 (2015) 261-269.

[38] G. Liao, S. Chen, X. Quan, H. Yu, H. Zhao, Graphene oxide modified g-C_3N_4 hybrid with enhanced photocatalytic capability under visible light irradiation, J. Mater. Chem. 22 (2012) 2721-2726.

[39] Z.W. Tong, D. Yang, T.X. Xiao, Y. Tian, Z.Y. Jiang, Biomimetic fabrication of g-C_3N_4/TiO_2 nanosheets with enhanced photocatalytic activity toward organic pollutant degradation, Chem. Eng. J. 260 (2015) 117-125.

[40] Y. Wang, R. Shi, J. Lin, Y.F. Zhu, Enhancement of photocurrent and photocatalytic activity of ZnO hybridized with graphite-like C_3N_4, Energy Environ. Sci. 4 (2011) 2922-2929.

[41] Z.W. Tong, D. Yang, J.F. Shi, Y.H. Nan, Y.Y. Sun, Z.Y. Jiang, Three-dimensional porous aerogel constructed by g-C_3N_4 and graphene oxide nanosheets with excellent visible-light photocatalytic performance, ACS Appl. Mater. Interfaces, 7 (46) (2015) 25693-25701.

[42] Z. Huang, Q. Sun, K. Lv, Z.H. Zhang, M. Li, B. Li, Effect of contact interface between TiO_2 and g-C_3N_4 on the photoreactivity of g-C_3N_4/TiO_2 photocatalyst: (0 0 1)

vs (1 0 1) facets of TiO_2, Appl. Catal. B: Environ. 164 (2015) 420-427.

[43] Y.G. Su, Y.X. Zhao, Y.J. Zhao, J.Y. Lang, X. Xin, X.J. Wang, Novel ternary component Ag-$SrTa_2O_6$/g-C_3N_4 photocatalyst: Synthesis, optical properties and visible light photocatalytic activity, Appl. Surf. Sci. 358 (2015) 213-222.

[44] Y.Y. Bu, Z.Y. Chen, Effect of oxygen-doped C_3N_4 on the separation capability of the photoinduced electron-hole pairs generated by O-C_3N_4@TiO_2 with quasi-shell-core nanostructure, Electrochim. Acta 144 (2014) 42-49.

[45] A. Ishikawa, T. Takata, J.N. Kondo, M. Hara, K. Domen, Electrochemical Behavior of Thin Ta_3N_5 Semiconductor Film, J. Phys. Chem. B 108 (2004) 11049-11053.

[46] G.H. Dong, L.Z. Zhang, Porous structure dependent photoreactivity of graphitic carbon nitride under visible light, J. Mater. Chem. 22 (2012) 1160-1166.

[47] L.H. Tana, J.H. Xua, X.J. Zhang, Z.S. Hang, Y.Q. Jia, S.B. Wang, Synthesis of g-C_3N_4/CeO_2 nanocomposites with improved catalytic activity on the thermal decomposition of ammonium perchlorate, Appl. Surf. Sci. 356 (2015) 447-453.

[48] G. Hitoki, A. Ishikawa, T. Takata, J. N. Kondo, M. Hara, K. Domen, Ta_3N_5 as a novel visible light-driven photocatalyst, Chem. Lett. 31 (2002) 736-737.

[49] C. Liu, D. Yang, Y. Jiao, Y. Tian, Y.G. Wang, Z.Y. Jiang, Biomimetic synthesis of TiO_2-SiO_2-Ag nanocomposites with enhanced visible-light photocatalytic activity, ACS Appl. Mater. Interfaces 5 (2013) 3824-3832.

[50] Y. Zhang, Z.Y. Zhao, J.R. Chen, L. Cheng, J. Chang, W.C. Sheng, C.Y. Hu, S.S. Cao, C-doped hollow TiO_2 spheres: in situ synthesis, controlled shell thickness, and

superior visible-light photocatalytic activity, Appl. Catal. B: Environ. 165 (2015) 715-722.

[51] L.Y. Huang, H. Xu, Y.P. Li, H.M. Li, X.N. Cheng, J.X. Xia, Y.G. Xu, G.B. Cai, Visible light-induced WO_3/g-C_3N_4 composites with enhanced photocatalytic activity, Dalton Trans. 42 (2013) 8606-8616.

[52] M. Ou, Q. Zhong, S.L. Zhang, L.M. Yu, Ultrasound assisted synthesis of heterogeneous g-C_3N_4/$BiVO_4$ composites and their visible-light-induced photocatalytic oxidation of NO in gas phase, J. Alloys Compd. 626 (2015) 401-409.

[53] C.C. Chen, W.H. Ma, J.C. Zhao, Semiconductor-mediated photodegradation of pollutants under visible-light irradiation, J. Chem. Soc. Rev. 39 (2010) 4206-4219.

[54] P. Zhou, J.G. Yu, M. Jaroniec, All-solid-state Z-Scheme photocatalytic systems, Adv. Mater. 26 (2014) 4920-4935.

[55] Y.M. He, L.H. Zhang, B.T. Teng, M.H. Fan, New application of Z-Scheme Ag_3PO_4/g‑C_3N_4 composite in converting CO_2 to fuel, Environ. Sci. Technol. 49 (2015) 649-656.

[56] Y.F. Chen, W.X. Huang, D.L. He, Y. Situ, H. Huang, Construction of heterostructured g-C_3N_4/Ag/TiO_2 microspheres with enhanced photocatalysis performance under visible-light irradiation, ACS Appl. Mater. Interfaces 6 (2014) 14405-14414.

[57] J. Jiang, H. Li, L.Z. Zhang, New insight into daylight photocatalysis of AgBr@Ag: synergistic effect between semiconductor photocatalysis and plasmonic photocatalysis, Chem. Eur. J. 18 (2012) 6360-6369.

[58] J.G. Yu, S.H. Wang, J.X. Low, W. Xiao, Enhanced photocatalytic performance of direct Z-scheme g-C_3N_4-TiO_2 photocatalysts for the decomposition of formaldehyde in air, Phys. Chem. Chem. Phys. 15 (2013) 16883-16890.

[59] Y.Z. Hong, Y.H. Jiang, C.S. Li, W.Q. Fan, X. Yan, M. Yan, W.D. Shi, In-situ synthesis of direct solid-state Z-scheme V_2O_5/g-C_3N_4 heterojunctions with enhanced visible light efficiency inphotocatalytic degradation of pollutants, Appl. Catal. B: Environ. 180 (2016) 663-673.

[60]N. Tian, H.W. Huang, Y.H. Zhang, Mixed-calcination synthesis of $CdWO_4$/g-C_3N_4 heterojunction with enhanced visible-light-driven photocatalytic activity, Appl. Surf. Sci. 358 (2015) 343-349.

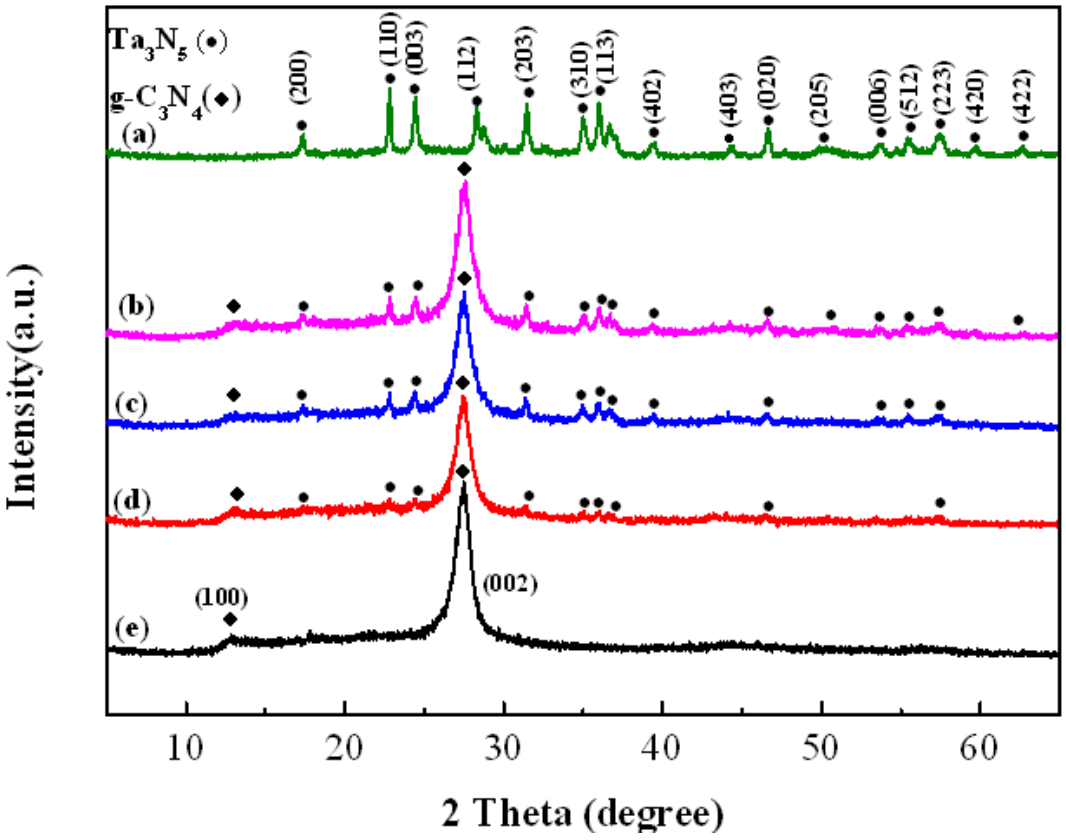

Fig. 1. XRD patterns of as-prepared photocatalysts: (a) Ta_3N_5; (b) 3-Ta_3N_5/g-C_3N_4; (c) 2-Ta_3N_5/g-C_3N_4; (d) 1-Ta_3N_5/g-C_3N_4; (e) g-C_3N_4.

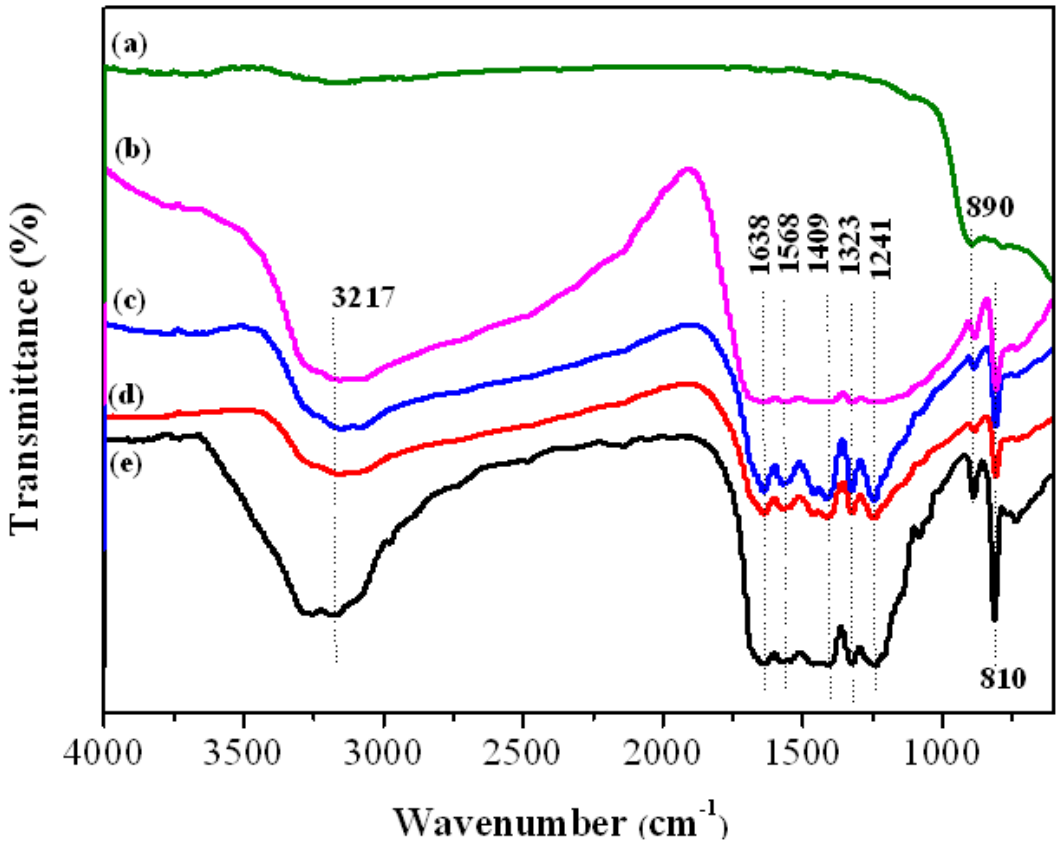

Fig. 2. FTIR spectra of as-prepared samples: (a) Ta_3N_5; (b) 3-Ta_3N_5/g-C_3N_4; (c) 2-Ta_3N_5/g-C_3N_4; (d) 1-Ta_3N_5/g-C_3N_4; (e) g-C_3N_4.

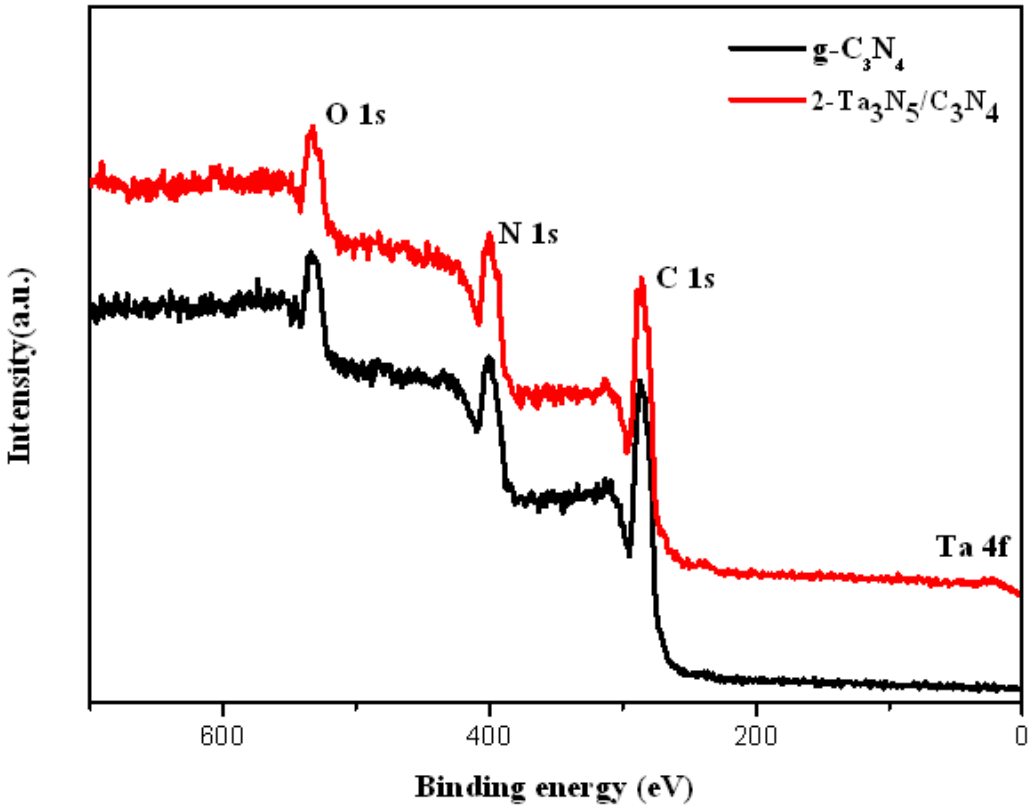

Fig. 3. XPS survey spectra of g-C_3N_4 and 2-Ta_3N_5/g-C_3N_4 photocatalysts.

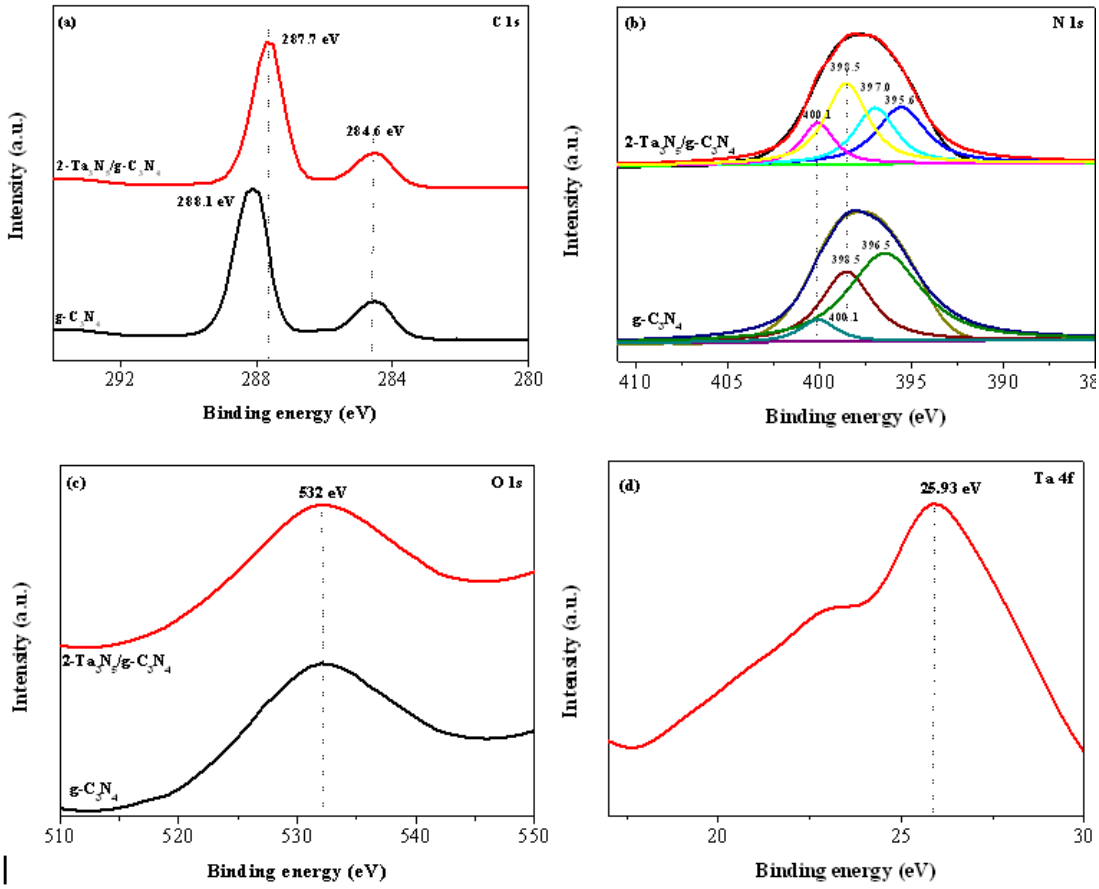

Fig. 4. High-resolution XPS spectra of samples: (a) C 1s, (b) N 1s and (c) O 1s of g-C_3N_4 and 2-Ta_3N_5/g-C_3N_4 samples, (d) Ta 4f of 2-Ta_3N_5/g-C_3N_4 composite.

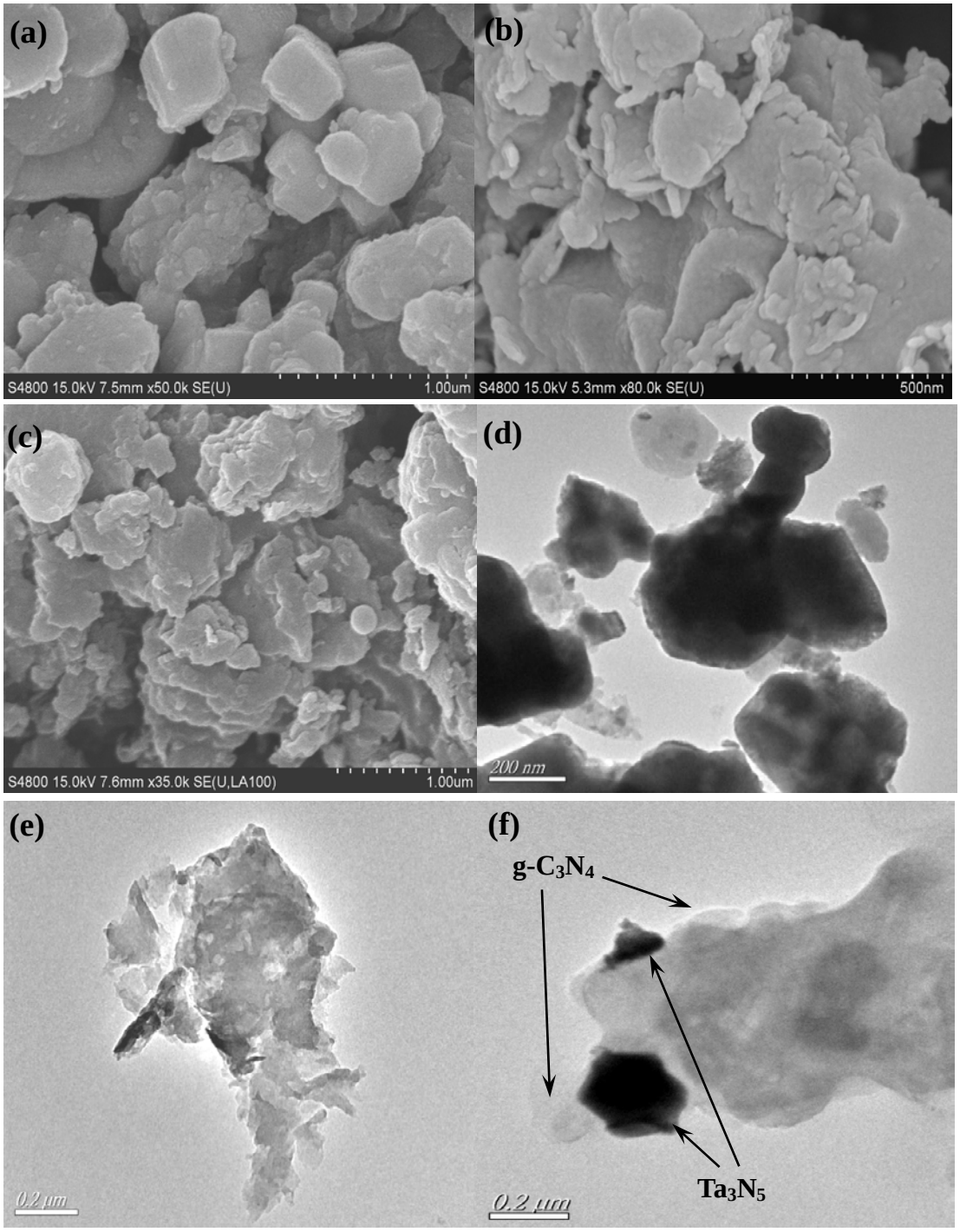

Fig. 5. FE-SEM images of samples: (a) Ta_3N_5, (b) g-C_3N_4, (c) 2-Ta_3N_5/g-C_3N_4, and TEM images of (d) Ta_3N_5, (e) g-C_3N_4 and (f) 2-Ta_3N_5/g-C_3N_4.

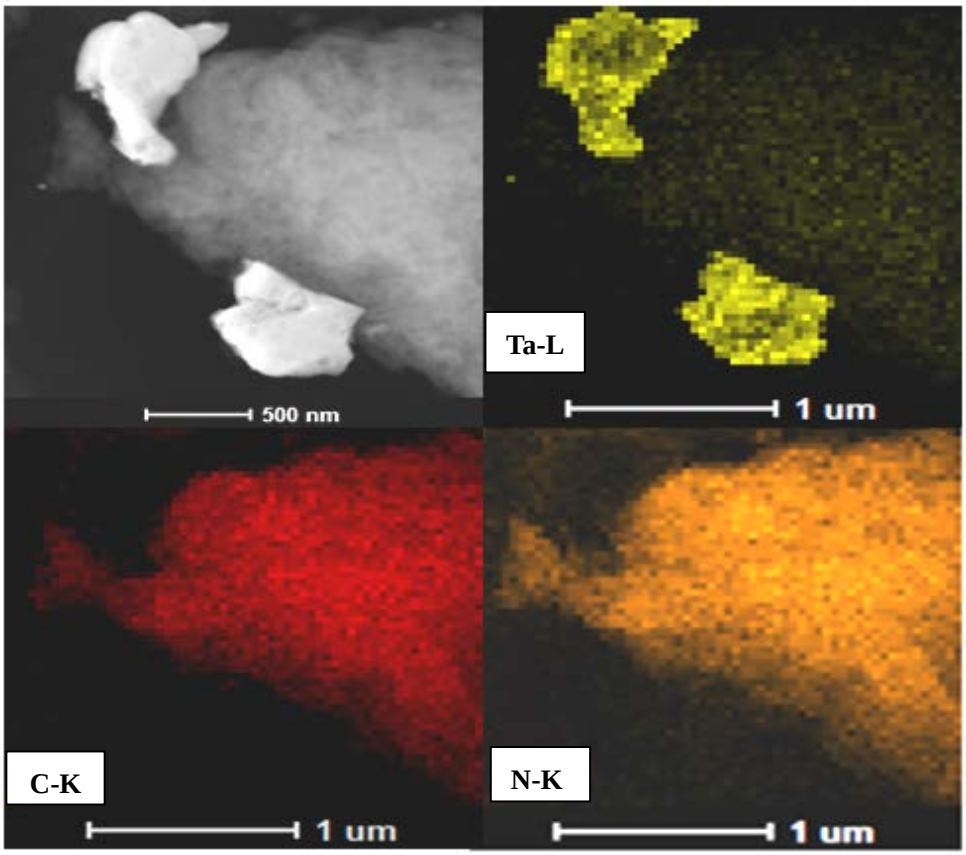

Fig. 6. HAADF-STEM images of the 2-Ta_3N_5/g-C_3N_4 sample with EDS maps of C-K, N-K, and Ta-L.

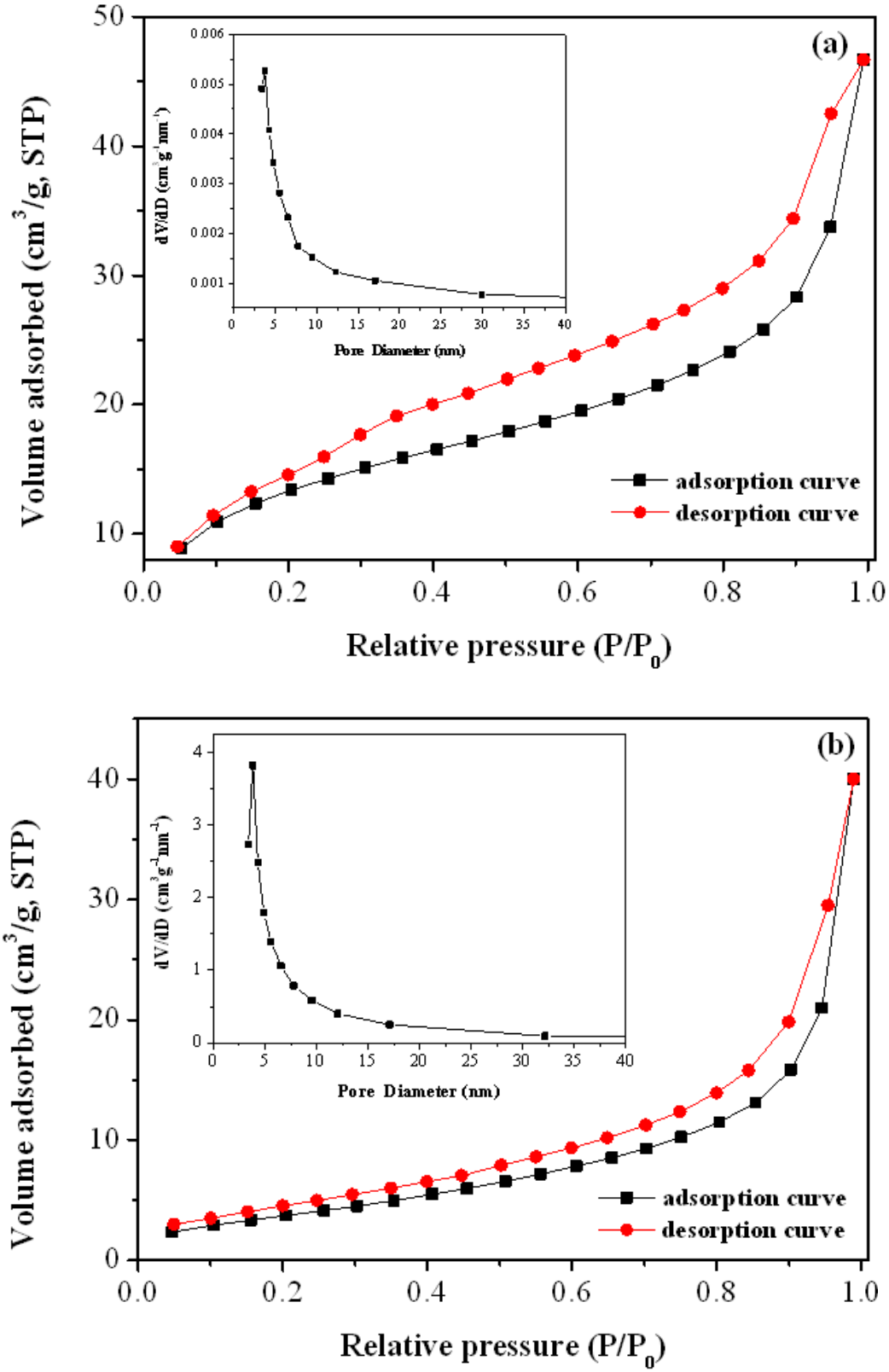

Fig. 7. Nitrogen sorption isotherms and corresponding Barrett-Joyner-Halenda (BJH) pore size distribution plots (inset) of (a) g-C_3N_4 and (b) 2-Ta_3N_5/g-C_3N_4.

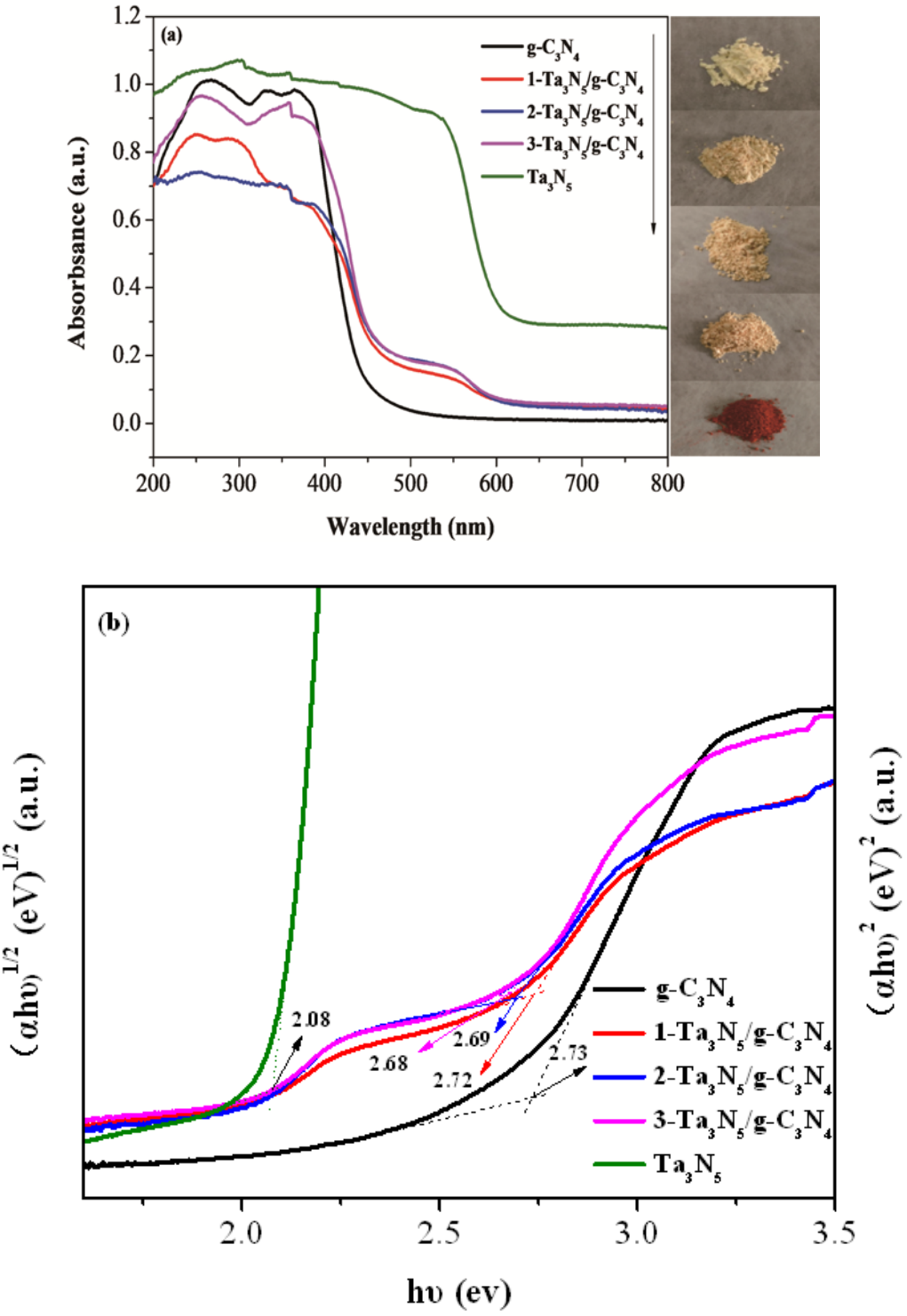

Fig. 8. (a) UV-vis diffuse reflection spectra of as-prepared photocatalysts; (b) the plots of the $(\pm h\nu)^{1/2}$ vs photon energy ($h\nu$) for g-C_3N_4 and X-Ta_3N_5/g-C_3N_4 (X=1,2,3) and a plot of the $(\pm h\nu)^2$ vs photon energy ($h\nu$) for Ta_3N_5.

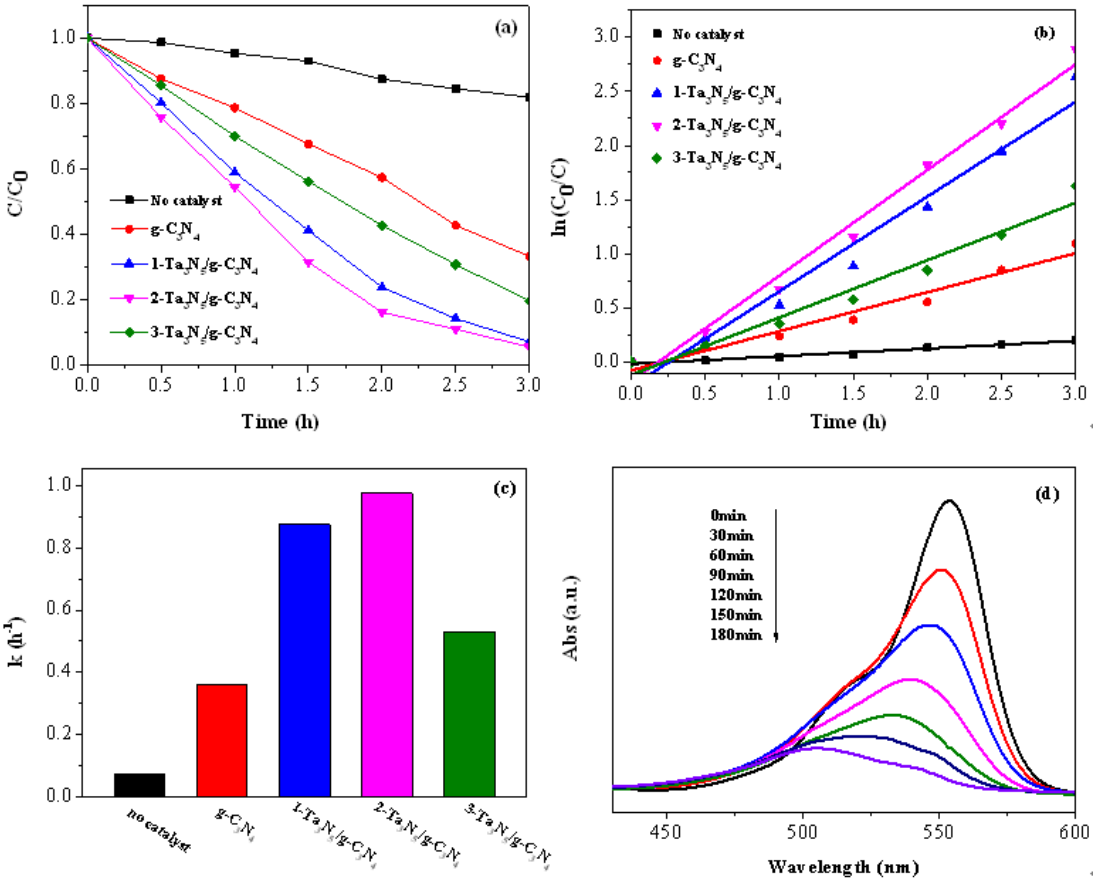

Fig. 9. (a) Photocatalytic degradation of RhB in the presence of as-prepared samples under visible light irradiation; (b) first-order kinetics data for the photodegradation of RhB over as-synthesized composites; (c) the apparent rate constants for RhB degradation; (d) temporal UV-vis absorption spectral changes of RhB in aqueous solution over 2-Ta_3N_5 /g-C_3N_4 photocatalyst.

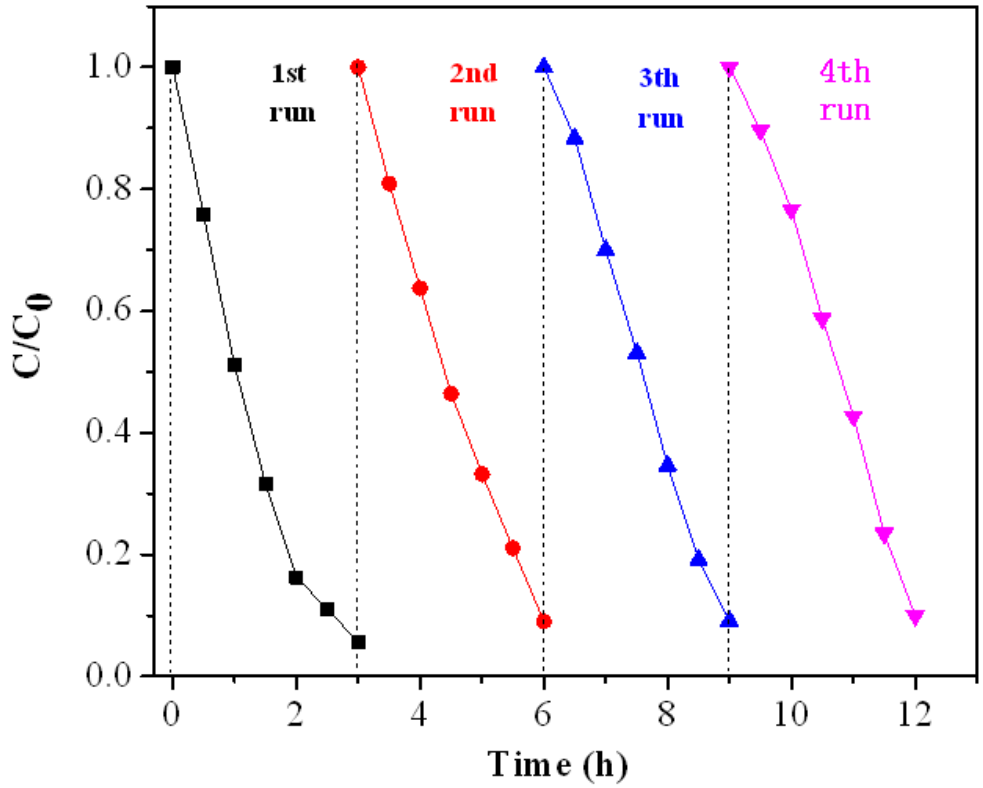

Fig. 10. Cycling runs in photocatalytic degradation of RhB over 2-Ta_3N_5/g-C_3N_4 photocatalyst under visible light irradiation.

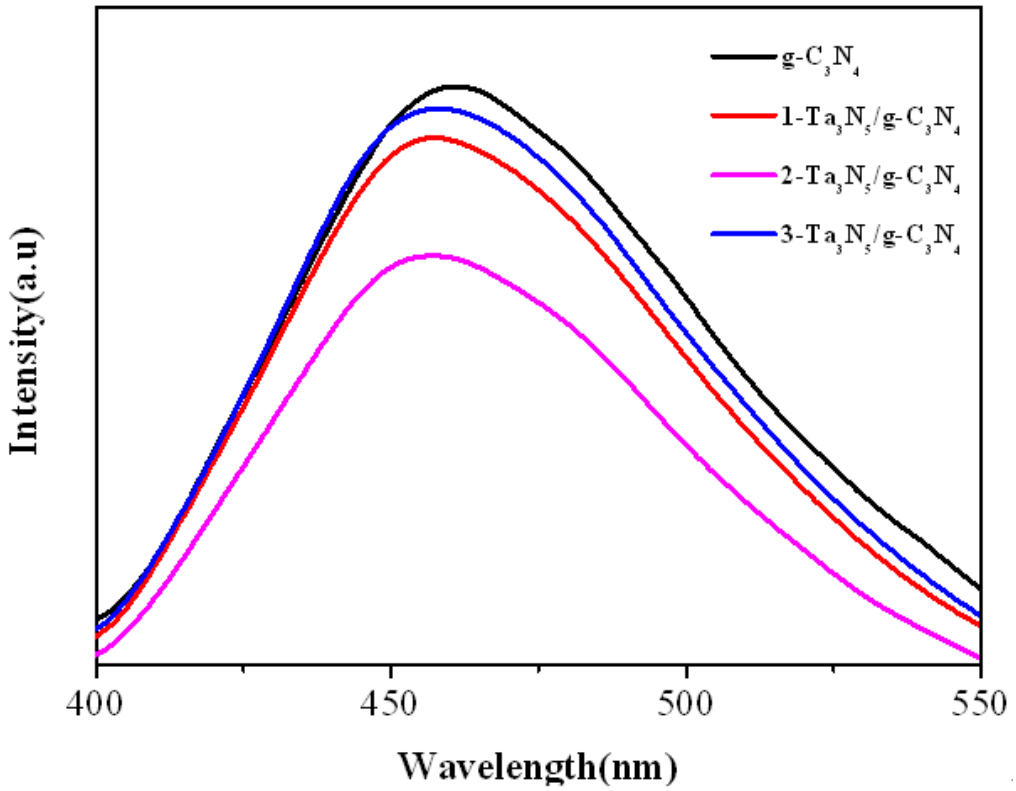

Fig. 11. Room temperature photoluminescence (PL) spectra of as-prepared samples.

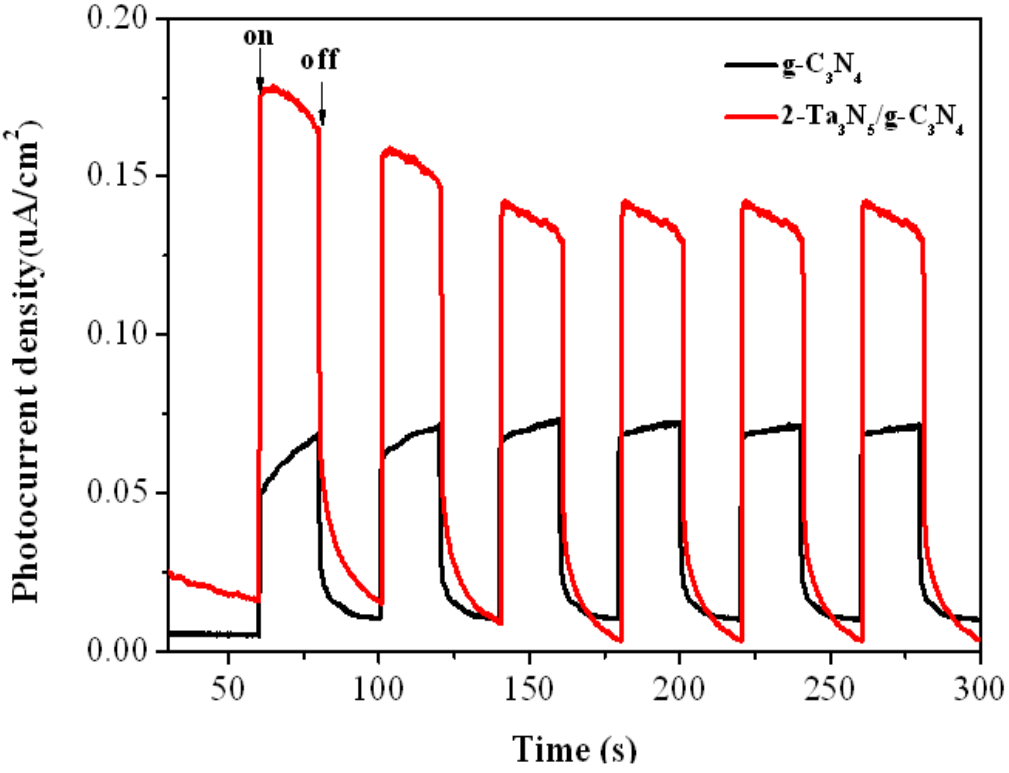

Fig. 12. Transient photocurrent responses of pure g-C_3N_4 and 2-Ta_3N_5/g-C_3N_4 under visible light irradiation.

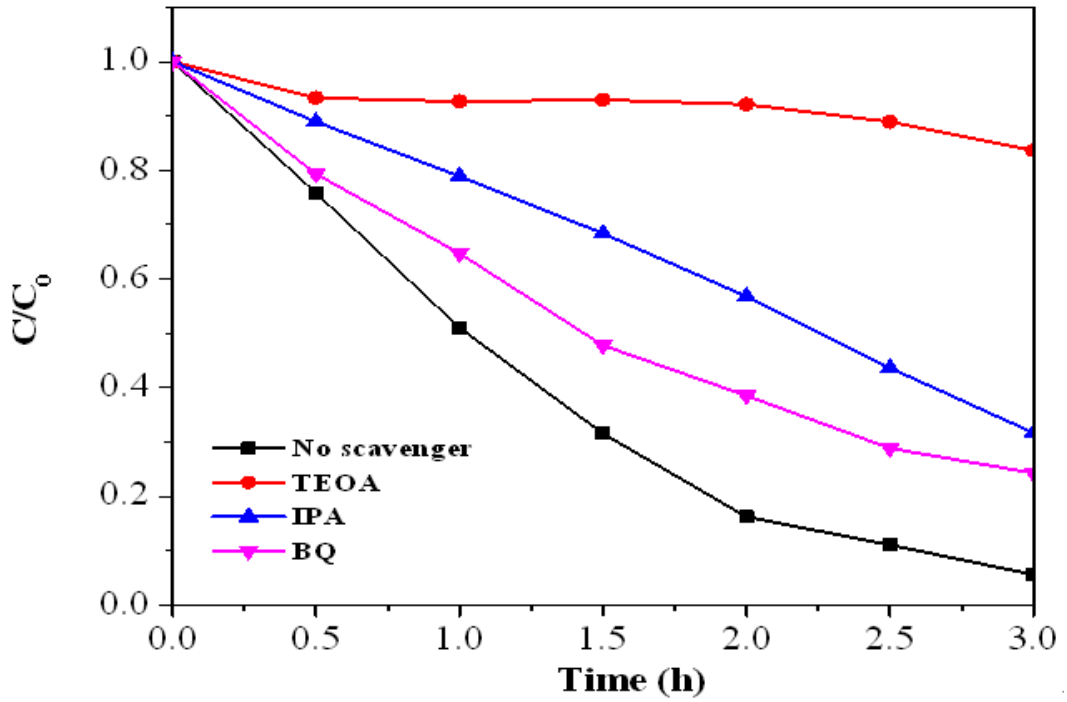

Fig. 13. Trapping experiments of active species during the photocatalytic degradation of RhB over 2-Ta_3N_5/g-C_3N_4 catalyst under visible light irradiation.

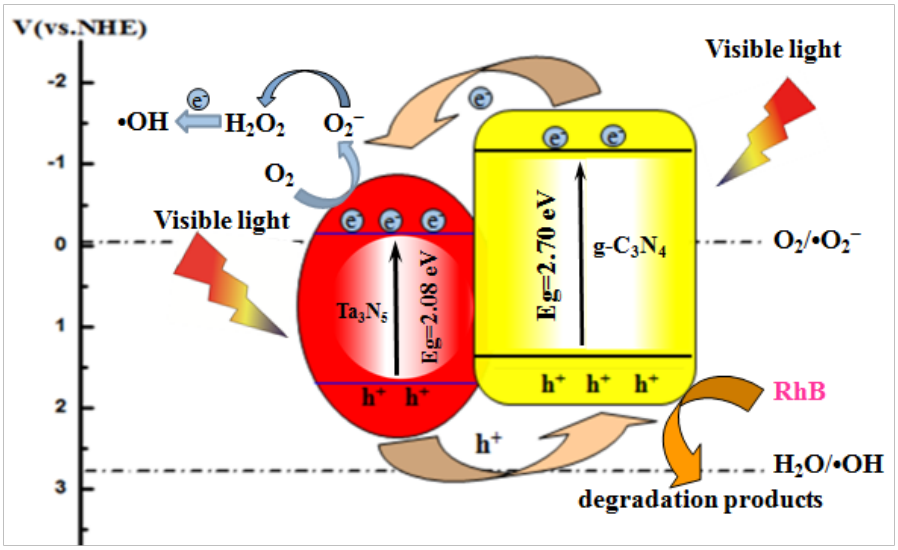

Fig. 14. Proposed photocatalytic mechanism of the charge transfer and RhB photodegradation in Ta_3N_5/g-C_3N_4 hybrids under visible light irradiation.

Table 1Measured BET parameters ofg-$C_3N_4$and 2-Ta_3N_5/g-C_3N_4hybrid photocatalysts.

Sample	Surfacearea (m^2g^{-1})	Porevolume (cm^3 g^{-1})	Averagepore size (nm)
g-C_3N_4	47.813	0.045	3.829
2-Ta_3N_5/g-C_3N_4	14.475	0.060	3.823